


## Surfing the capillary wave: Wetting dynamics beneath an impacting drop

John M. Kolinski,<sup>1</sup> Ramin Kaviani,<sup>1</sup> Dylan Hade,<sup>1</sup> and Shmuel M. Rubinstein <sup>2</sup>

<sup>1</sup>*École Polytechnique Fédérale de Lausanne, 1015 Lausanne, Switzerland*

<sup>2</sup>*The Paulson School of Engineering and Applied Sciences, Harvard University, Cambridge, Massachusetts 02138, USA*



(Received 8 October 2015; published 24 December 2019)

The initiation of contact between liquid and a dry solid is of great fundamental and practical importance. We experimentally probe the dynamics of wetting that occur when an impacting drop first contacts a dry surface. We show that, initially, wetting is mediated by the formation and growth of nanoscale liquid bridges, binding the liquid to the solid across a thin film of air. As the liquid bridge expands, air accumulates and deforms the liquid-air interface, and a capillary wave forms ahead of the advancing wetting front. This capillary wave regularizes the pressure at the advancing wetting front and explains the anomalously low wetting velocities observed. As the liquid viscosity increases, the wetting front velocity decreases; we propose a phenomenological scaling for the observed decrease of the wetting velocity with liquid viscosity.

DOI: [10.1103/PhysRevFluids.4.123605](https://doi.org/10.1103/PhysRevFluids.4.123605)

### I. INTRODUCTION

The impact of a drop upon a surface is a ubiquitous phenomenon in our daily experience, and plays a vital role in a plethora of natural and industrial processes. Applications range from deposition of inks, resins, and coatings to understanding why drops splash upon violent impact. Recent investigations into the influence of ambient air on droplet impact dynamics establish the critical effect the gas has on the outcome of the liquid-solid impact process, including suppression of splashing [1–4], a liftoff transition in the liquid-air interface [5], and complete rebound of the drop from a hydrophilic surface [6–8], adding to our understanding of the role of air in droplet impacts [9–14]. As a prelude to wetting, the impinging liquid first compresses the air beneath the drop into a dimple [15–18], and subsequently confines the intervening air into a nanometer-thin film circumscribing the dimple region [5, 19–21]. The dynamics at the leading edge of the spreading liquid have been shown to be distinct from the dimple region and are important for droplet spreading and splashing [13, 22, 23]. On ideal surfaces, such as freshly cleaved mica, contact occurs when the thickness of the thin air film reaches a few nanometers, and the interface is destabilized by surface forces [6]. On typical surfaces, defects nucleate contact much earlier; thus, liquid-solid contact initiates by the formation of a capillary bridge, linking the solid and liquid. The liquid bridge grows as the fluid rapidly wicks through the thin film of air, binding the drop to the surface [6, 19, 21]. These dynamics lead to the onset of wetting and bear remarkable similarity to dewetting studies on solid surfaces [24] and freely suspended viscous films [25], with key differences introduced by the nanometer-thin air film. In order for the nascent contact to grow, the spreading liquid must fully displace the air beneath the drop ahead of the propagating contact line. Indeed, recent simulations of dynamic wetting underscore the overwhelming difficulty of predicting the role of liquid viscosity in the wetting process due to the complicated flow patterns occurring across many scales [26].

Here, we directly examine the initial stages in the formation of liquid solid contact beneath the impacting drop and resolve the liquid-air interface kinematics over six orders of magnitude of spatial scales, from nanometers to millimeters, by using total internal reflection (TIR) microscopy.

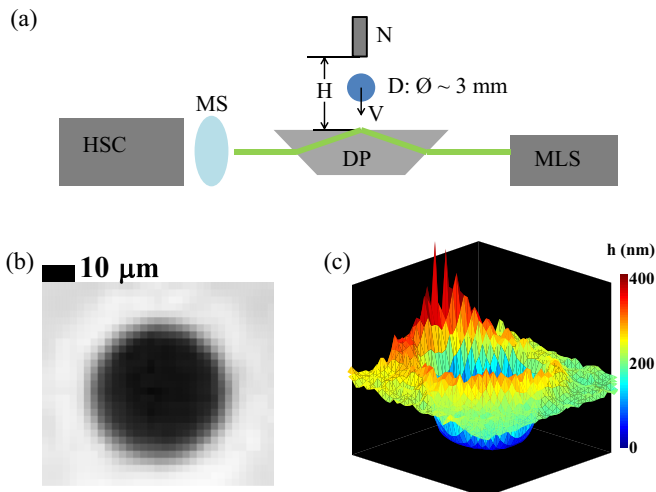


FIG. 1. High-speed TIR imaging of the initiation of wetting: (a) Collimated, monochromatic light (MLS) totally internally reflects off of the glass-air interface (DP). The angle of incidence is tuned such that, for a glass-liquid interface, light no longer obeys the conditions for total internal reflection and instead transmits through a wet glass. Reflected light exiting the prism is magnified with a long-working-distance microscope objective (MS) and is imaged on our fast camera’s imaging sensor (Phantom V711) (HSC) at up to 180 000 frames per second. (b) A typical TIR image of a capillary bridge formed beneath the thin film of air approximately 500 microns from the center of the impact. The height profile of the liquid above the solid surface can be calculated from the recorded intensity. (c) Three-dimensional rendering of the height map for the contact patch shown in (b). The color bar indicates the height above the glass surface.

High-speed TIR microscopy enables us to probe the wetting process beneath the impacting drop with exceptional spatial and temporal resolution and facilitates the full three-dimensional imaging of the advancing contact line and the nanometer-thin film of air that initially separates the liquid from the solid.

## II. METHODS

Drops with viscosities varying over two orders of magnitude are released from a syringe tip and impact upon a smooth glass surface. We used solutions of water and glycerol to obtain fluids with viscosities ranging from 1 to 100 cSt at room temperature. In each of these experiments, the droplet diameter is approximately 3 mm and the impact velocity is between 0.5 and 0.7 m/s, corresponding to an impact Weber number with a range of 5.2–13.9, calculated based on the droplet radius. In this regime, the air film initially established during impact varies from approximately 300 to several tens of nanometer in thickness [6]. As shown in Fig. 1(a), to visualize the liquid-air interface, we illuminate the upper surface of a dove prism from below with a collimated, monochromatic light source at an angle of incidence greater than the total internal reflection angle for a glass-air interface, thus exciting an exponentially decaying evanescent field immediately above the glass surface. Any liquid that enters the evanescent field above the surface will allow the light to partially transmit into it. Previous experiments in our group using the technique [5,6,19] employed a total-energy transfer algorithm to invert the intensity data to height. However, such a transfer algorithm does not account for the polarization of the light [27]. More recent work from the physics of fluids group in Twente [28] clarifies that the transfer function from recorded intensity to height must account for the polarization of the light. We include a supplementary figure showing how the former intensity inversion compares with the corrected inversion algorithm in the supplementary information [29]. By imaging the light after it exits the prism with our camera’s imaging sensor, we

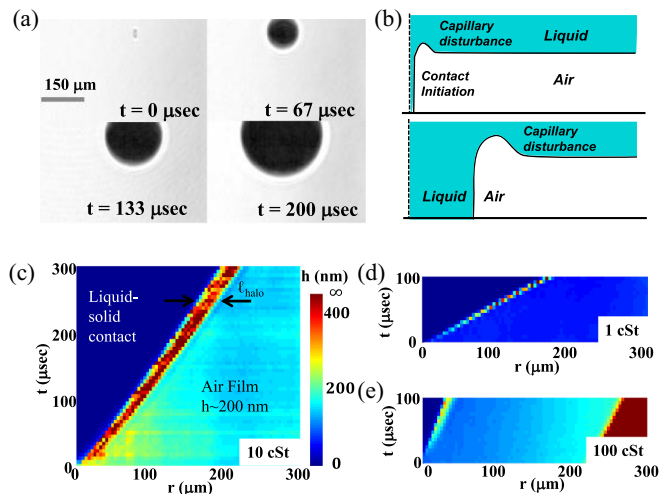


FIG. 2. Initiation and growth of liquid-solid contact: (a) A sequence of TIR images showing the initiation of contact between the glass surface and a  $10$  cSt liquid drop. At  $t = 0$ , the contact first forms. As time progresses, the contact line moves symmetrically out from the initial point of contact formation. The air ahead of the advancing wetting front fails to drain and instead deforms the liquid-air interface. Consequently, a bright “halo” surrounds the liquid bridge. (b) A schematic representing the  $r$ - $z$  plane normal to the impact surface demonstrates how the halo region grows ahead of the advancing contact. As mentioned in the Supplemental Material [29], the conformation of the liquid-air interface (dashed line) cannot be resolved below one micron with the TIR method, limiting our ability to resolve the profile within nanometers of the contact line. (c) The azimuthally averaged height profiles are plotted in a kymograph for  $10$  cSt liquid. The contact line progresses outward with a nearly constant velocity, and the lateral extent of the halo grows over time, as indicated by the widening of the bright red region. (d) A kymograph of liquid-solid contact initiation beneath a  $1$  cSt liquid drop shows similar, albeit more rapid, dynamics. (e) A kymograph of liquid-solid contact beneath a  $100$  cSt liquid drop. Here, the contact line moves with a slower velocity.

are not light limited, and indeed we can perform ultrahigh-speed imaging in order to reconstruct the three-dimensional profile of the liquid-air interface, as shown in Figs. 1(b) and 1(c).

### III. RESULTS

While the rms roughness of the glass slides is of the order of nanometers, sparsely distributed defects on the glass surface will exceed tens or even hundreds of nanometers in height above the surface [4,6]; these protrusions may therefore exceed the thickness of the thin film of air above the surface of the glass and thus act as nucleation sites for the formation of a capillary nanobridge. These sparse nuclei are the dominant mechanism for contact initiation in most realistic systems [6,19]. We characterize the initial dynamics of wetting by analyzing images of the TIR intensity captured with our fast camera. For all the fluid viscosities and film thicknesses that we examined, the initial formation of a solid-liquid contact region occurs in a qualitatively similar manner, as shown for a typical example in Fig. 2(a). Initially, a point-like contact forms beneath the thin film of air; simultaneously, a capillary disturbance is excited at the liquid-air interface wherein the displaced air is driven. This feature reduces the radius of curvature of the interface ahead of the advancing contact line, thus reducing the capillary pressure. The initiation and growth of the capillary disturbance are shown schematically in Fig. 2(b). This disturbance appears in the TIR images as a bright region, or *halo*, encircling the dark spot, which indicates the wetted area. The contact angle between the liquid and the glass is small and, therefore, once the contact is formed, the wetting front rapidly

spreads laterally outward at an approximately constant velocity, eventually reaching the boundary of the thin film of air.

Before the spreading contact line can progress, it must first displace the air in its path; however, the hydrodynamic resistance of the air, which is confined in the thin gap beneath the drop, is very high. Similar flow conditions occur at the onset of droplet coalescence, but the boundary conditions are fundamentally distinct [30,31]. The capillary number,  $Cp = \frac{V\mu}{\gamma}$ , for this flow is very small, suggesting that the air viscosity plays a negligible role; however, this does not account for the confinement of the air in the thin film beneath the impacting drop: here, the thin gap amplifies resistance to the flow of the air. The deformation of the liquid from the formation of the halo leads to the development of a Laplace pressure, and consequently a pressure drop toward the edge of the spreading droplet, where the pressure is atmospheric; this pressure drop is  $\Delta p \sim 0.01\text{--}0.1$  atm. As a result of the air's strong confinement upon impact, this pressure drop is insufficient to expel the air ahead of the advancing contact line [32]. Instead, the air accumulates and forces the liquid-air interface to rise and curve at the leading edge, effectively inflating a toroidal bubble.

As the liquid bridge expands and the contact region continuously grows, the halo also grows to accommodate the increasing volume of displaced air, similar to classical inertial and viscous dewetting [33]. The dynamics of the expanding bridge are summarized as a function of space and time for three viscosities in the kymographs shown in Figs. 2(c)–2(e).  $t = 0, r = 0$ , indicate the center of the initial contact point. The growing dark region on the left side of the plots corresponds to the wetted area, labeled “liquid-solid contact” in Fig. 2(c). Similar dynamics are observed for the full range of measured viscosities, up to 100 cSt, as shown in Figs. 2(d) and 2(e). For higher-viscosity liquids, the wetting front proceeds more slowly than for lower-viscosity liquids; however, the shape of the profile of the air film ahead of the wetting front is qualitatively similar for all air film thicknesses and all liquid viscosities.

At the earliest stages of contact formation and growth, we directly observe the three-dimensional geometry of the liquid-air interface and measure both the height  $dh$  and breadth  $\ell_{\text{halo}}$  of the deformed interface surrounding the liquid bridge, as shown in the height profiles  $h(r)$  in Fig. 3(a). The gas film thickness  $h_{\text{film}}$  remains nearly constant as the wetting front progresses [6], as can be seen by the overlap of the successive profiles at large  $r$ . For an ensemble of many droplet impacts, we find that the lateral scale of the halo feature  $\ell_{\text{halo}}$  grows slowly in time and at the same rate, independent of viscosity, as shown in Fig. 3(b). Whereas typically  $dh$  rapidly exceeds the submicron resolution of the TIR imaging modality, we are able to directly measure this height at the earliest stage of the capillary nanobridge for the highest viscosities. The halo shape is robust and does not measurably deform; this can be understood by the capillary number for flow in the air, which at the highest contact line velocities is approximately  $Cp \sim 10^{-4}$ ; thus surface tension maintains the shape of the propagating halo [33]. For the earliest instants of contact formation, we also compute the predicted halo height,  $dh_p = \frac{h_{\text{film}}r}{\ell_{\text{halo}}}$ , and compare it to the measured halo height  $dh_m$ , finding good agreement for most viscosities, with an overprediction for the lowest viscosity measured. While the measured and predicted values for  $dh$  nearly agree, we see that the measurement is consistently less than the predicted value, implying that the air is either slowly draining or compressing; however, the capillary stresses correspond to a fraction of a percent of an atmosphere, suggesting that the air is in fact slowly draining from beneath the impacting droplet.

As the liquid bridge spreads, the contact line velocity  $v$  remains approximately constant, as shown for three different viscosities in Fig. 2. As previously stated, similar dynamics are observed during droplet coalescence, where the expanding neck grows at a constant rate before a transition to slower growth [30]; here, our boundary conditions are different, and we do not see a transition, but instead the contact grows at a nearly constant velocity. This velocity does not appear to depend on the air film thickness through which it propagates. Under these conditions, for pure water the capillary pressure generated by a capillary bridge across an air film of 100 nm would rapidly accelerate the contact line to the limiting velocity, given by the balance of inertial and capillary stresses [34],  $v = \sqrt{\gamma/(\rho h)} = 26$  m/s. For  $h = 10$  nm,  $v = 83$  m/s, this velocity will even exceed

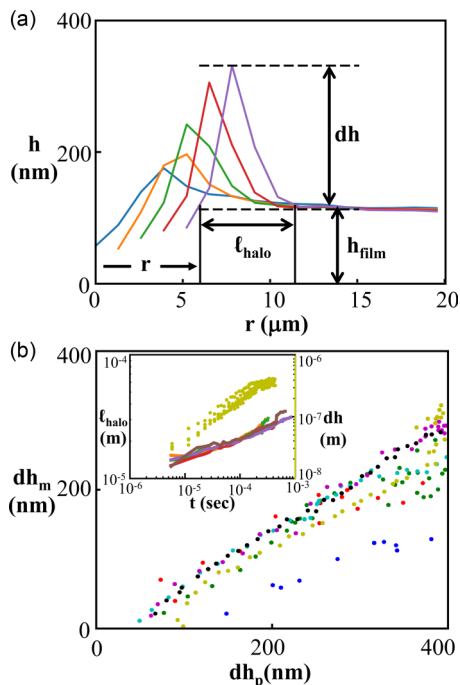


FIG. 3. Kinematics of the wetting front: (a) Five consecutive height profiles ( $dt = 5.5 \mu\text{s}$ ) of a wetting front propagating outward from the point of contact initiation. The halo region leading the propagating front excites a capillary wave ahead of it, with a lateral extent  $\ell_{\text{halo}}$  and vertical dimension  $dh$ . The front position  $r_c$  is defined as the location where the wetting front reaches the height of the film in the far field  $h_{\text{film}}$ . (b) The volume of air displaced by the advancing wetting front, assuming the air is incompressible, can be used to develop a prediction for  $dh$ ,  $dh_p = rh_{\text{film}}/\ell_{\text{halo}}$ . The measured value of  $dh$ ,  $dh_m$ , is obtained via TIR measurements immediately after contact initiation, and compares favorably with  $dh_p$ , as can be seen by the direct relationship between these quantities. Inset:  $\ell_{\text{halo}}$  as a function of  $t$ ; colors represent different viscosities.  $\ell_{\text{halo}}$  grows slowly in time; no systematic dependence of  $\ell_{\text{halo}}$  is found as  $\nu$  is varied. The height of the halo feature  $dh$  increases in time, as shown here for  $\nu = 76$  cSt liquid, as can be seen by the gold points corresponding to the axis on the right-hand side of the plot.

the liquid-capillary limit set by  $\gamma/\eta = 70$  m/s! However, we observe entirely different dynamics: here, the wetting front propagates more than an order of magnitude slower, and at the same speed  $v$  through a 10-nm-thick film of air as through a 100-nm-thick film of air, and is thus insensitive to the air film thickness. This suggests that liquid inertia alone does not limit  $v$ , and that dynamics of contact initiation and growth are significantly altered by the halo region ahead of the advancing contact line.

The anomalously low measured values of  $v$  points to an alternative mechanism of contact line motion through the thin film of air. To understand how a wetting front spreads, we consider the flow near the contact line, shown schematically in Fig. 4(a). The air ahead of the contact line cannot drain fast enough through the thin gap and instead accumulates in the halo. The contact line advances, driven by wetting forces; however, it must also be accommodated by flow of the liquid along the liquid-air interface. This flow must bypass the halo, which acts as a geometrical disturbance. Thus, the contact line is effectively *dragging* the halo through the drop's lower surface. This provides added inertial resistance to the motion of the contact line and limits spreading speeds to that of a capillary wave, or the rate at which a disturbance with a typical scale  $\ell_{\text{halo}}$  can move on the surface of the liquid as the contact line advances. However, the formation of the halo at the leading edge of the

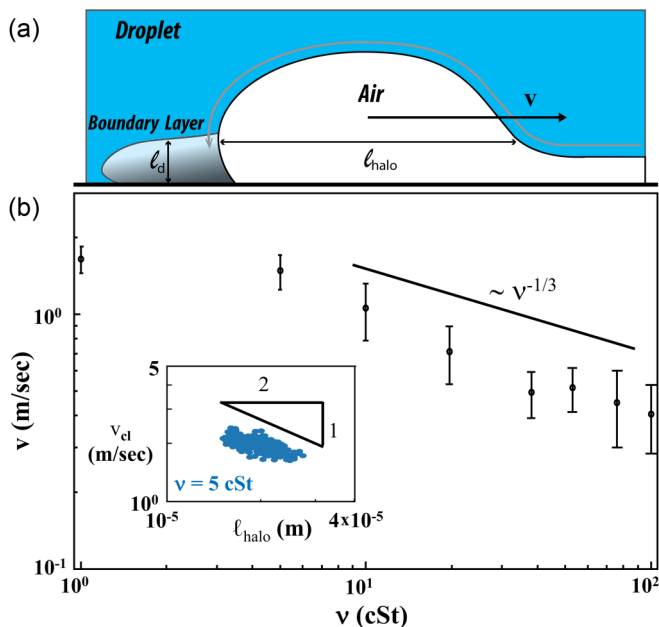


FIG. 4. Surfing on a capillary wave: (a) A schematic of the spreading capillary bridge. Fluid is shown in blue, the halo region and thin film of air are shown in white, and the surface is indicated by the black solid line. Viscous dissipation is localized in a boundary layer, indicated by the region trailing the contact line. (b) The average contact line velocity is plotted as a function of liquid viscosity; error bars indicate standard deviation of all contact events. Mean velocity decreases as a nonlinear function of liquid viscosity. Inset: over a small range, the velocity varies inversely with  $\ell_{\text{halo}}$  for the 5 cSt liquid, consistent with the predicted scaling for a capillary wave.

contact line leads to a resistance fundamentally dissimilar from classical dewetting films [33,35,36]. Here, the contact line is resisted also by the inertia of the fluid displaced by the air in the halo.

The breadth of the halo region varies slowly and thus we can estimate a wave number corresponding to the average length of  $\langle \ell_{\text{halo}} \rangle_t = 20 \mu\text{m}$ , and the velocity of such capillary disturbances given by  $c = \sqrt{\frac{2\pi\gamma}{\rho\ell_{\text{halo}}}}$ , where  $c$  is the wetting velocity [33]. Substituting the typical value of  $\ell_{\text{halo}} = 20 \mu\text{m}$  into this expression, we find that  $c = 4.3 \text{ m/s}$ , which has the same order of magnitude as the velocity of the lowest viscosity 1 cSt water-glycerol solution that we measured.

To check whether the capillary-wave argument has experimental support, we can use the predicted relationship between  $c$  and  $\ell_{\text{halo}}$  in the inertial limit, where  $c \propto \ell_{\text{halo}}^{-1/2}$ . The velocity is nearly constant, as shown in Fig. 2, and  $\ell_{\text{halo}}$  varies extremely slowly as shown in Fig. 3; nevertheless, these quantities do vary slightly over the course of the experiment. For the 5 cSt liquid, the contact line velocity appears to vary inversely with  $\ell_{\text{halo}}$ , as shown in Fig. 4, inset. While the range of  $v$  and  $\ell_{\text{halo}}$  is insufficient to verify the predicted scaling, the nearly 500 data points shown indicate consistency with the capillary-wave argument.

#### IV. DISCUSSION

As the viscosity increases, the contact line velocity decreases. The wetting velocity does not seem to vary strongly with viscosity for the lowest viscosity values, but our data density at these lower viscosity values is insufficient to comment on whether this is a distinctive regime, and how it might transition to a viscous-dominated regime observed for higher viscosities as shown in Fig. 4(b).

How will the spreading velocity change for a more viscous fluid? The halo region introduces a new length scale for the flow at the advancing wetting front. Typically the dissipation at the contact line should occur on the scale of the flow; our observed  $\ell_{\text{halo}}$  length scale is the only candidate scale here, and thus the volume wherein the dissipation occurs should be  $r\ell_{\text{halo}}^2$ . This scaling suggests that the contact line velocity should scale as the square root of the radius, which is inconsistent with observations, so we introduce a scaling that incorporates a viscous boundary layer. The flow around the halo is inertial [37], but close enough to the contact line the fluid flows on scales that are sufficiently small for the dynamics to be dominated by viscous dissipation. Dissipation is nevertheless confined to a boundary layer along the solid-liquid interface, and the propagation dynamics are governed by the balance of viscous and capillary stresses:

$$\frac{\gamma}{\rho\ell_{\text{halo}}} \sim v \frac{v}{\ell_d},$$

where  $\ell_d \sim \sqrt{\nu\tau}$  is the length-scale over which dissipation occurs and is determined by the time required for a boundary layer to develop  $\tau$ . Here we note that the dominant intrinsic length scale  $\ell_{\text{halo}}$  sets  $\tau \sim \frac{\ell_{\text{halo}}}{v}$ . The stress balance equation then reads:  $\frac{\gamma}{\rho\ell_{\text{halo}}} \sim \sqrt{\frac{v}{\ell_{\text{halo}}}} v^{3/2} \rightarrow v \sim \left(\frac{\gamma}{\rho\sqrt{v\ell_{\text{halo}}}}\right)^{2/3}$ . This suggests that the contact line velocity varies inversely with the kinematic viscosity, consistent with our measurements.

While our experiments were conducted at low impact velocities significantly below the splashing threshold, the observed wetting velocity might affect splashing, because viscous liquids typically eject their sheet at a much later stage of the dynamics, when contact through the air film is likely to have occurred [12]. When a drop approaches a solid surface, even at moderate velocities the initial dynamics of wetting are strongly altered by the confined air film, which is displaced by the wetting fluid and consequently deforms the liquid-air interface ahead of the contact line. The deformation results in a capillary disturbance that precedes the wetting front and leads to anomalously low wetting velocities beneath the impacting drop. These dynamics, ahead of the contact line, are inertial. Several nanometers below, trailing the contact line, a boundary layer is formed and the flow is viscous. These dynamically different regimes are coupled by the halo geometry, as on the one hand, the size of the boundary layer depends on the time it takes the wetting front to traverse the size of the halo. On the other hand, the size of the halo depends on the propagation speed of the contact line, which is driven by the extreme curvature and hindered by the trailing viscosity. Thus, the wetting front is surfing on a capillary wave and dragging a viscous tail in its wake.

#### ACKNOWLEDGMENTS

This work was supported by Harvard MRSEC (DMR 14-20570) and ISF Grant No. 1415/12. J.M.K. acknowledges support from the NSF GRFP graduate research fellowship, the Fulbright-Israel postdoctoral fellowship, and EMSI at EPFL.

- 
- [1] L. Xu, W. W. Zhang, and S. R. Nagel, Drop Splashing on a Dry Smooth Surface, *Phys. Rev. Lett.* **94**, 184505 (2005).
  - [2] S. Mandre, M. Mani, and M. P. Brenner, Precursors to Splashing of Liquid Droplets on a Solid Surface, *Phys. Rev. Lett.* **102**, 134502 (2009).
  - [3] M. Mani, S. Mandre, and M. P. Brenner, Events before droplet splashing on a solid surface, *J. Fluid Mech.* **647**, 163 (2010).
  - [4] S. Mandre and M. P. Brenner, The mechanism of a splash on a dry solid surface, *J. Fluid Mech.* **690**, 148 (2012).
  - [5] J. M. Kolinski, L. Mahadevan, and S. M. Rubinstein, Lift-Off Instability During the Impact of a Drop on a Solid Surface, *Phys. Rev. Lett.* **112**, 134501 (2014).

- [6] J. M. Kolinski, L. Mahadevan, and S. M. Rubinstein, Drops can bounce from perfectly hydrophilic surfaces, *Europhys. Lett.* **108**, 24001 (2014).
- [7] J. de Ruitter, R. Lagraauw, D. van den Ende, and F. Mugele, Wettability-independent bouncing on flat surfaces mediated by thin air films, *Nat. Phys.* **11**, 48 (2015).
- [8] J. de Ruitter, R. Lagraauw, F. Mugele, and D. van den Ende, Bouncing on thin air: How squeeze forces in the air film during non-wetting droplet bouncing lead to momentum transfer and dissipation, *J. Fluid Mech.* **776**, 531 (2015).
- [9] I. V. Roisman, R. Rioboo, and C. Tropea, Normal impact of a liquid drop on a dry surface: Model for spreading and receding, *Proc. R. Soc. London, Ser. A* **458**, 1411 (2002).
- [10] A. Yarin, Drop impact dynamics: Splashing, spreading, receding, bouncing, *Annu. Rev. Fluid Mech.* **38**, 159 (2006).
- [11] S. Chandra and C. T. Avedisian, On the collision of a droplet with a solid surface, *Proc. R. Soc. London, Ser. A* **432**, 13 (1991).
- [12] M. M. Driscoll, C. S. Stevens, and S. R. Nagel, Thin film formation during splashing of viscous liquids, *Phys. Rev. E* **82**, 036302 (2010).
- [13] M. M. Driscoll and S. R. Nagel, Ultrafast Interference Imaging of Air in Splashing Dynamics, *Phys. Rev. Lett.* **107**, 154502 (2011).
- [14] C. Josserand and S. T. Thoroddsen, Drop impact on solid surface, *Ann. Rev. Fluid Mech.* **48**, 365 (2015).
- [15] S. T. Thoroddsen, T. G. Etoh, and K. Takehara, Air entrapment under an impacting drop, *J. Fluid Mech.* **478**, 125 (2003).
- [16] S. T. Thoroddsen, T. G. Etoh, K. Takehara, N. Ootsuka, and Y. Hatsuki, The air bubble entrapped under a drop impacting on a solid surface, *J. Fluid Mech.* **545**, 203 (2005).
- [17] W. Bouwhuis, R. C. A. van der Veen, T. Tran, D. L. Keij, K. G. Winkels, I. R. Peters, D. van der Meer, C. Sun, J. H. Snoeijer, and D. Lohse, Maximal Air Bubble Entrainment at Liquid-Drop Impact, *Phys. Rev. Lett.* **109**, 264501 (2012).
- [18] J. S. Lee, B. M. Weon, J. H. Je, and K. Fezzaa, How Does an Air Film Evolve Into a Bubble During Drop Impact? *Phys. Rev. Lett.* **109**, 204501 (2012).
- [19] J. M. Kolinski, S. M. Rubinstein, S. Mandre, M. P. Brenner, D. A. Weitz, and L. Mahadevan, Skating on a Film of Air: Drops Impacting on a Surface, *Phys. Rev. Lett.* **108**, 074503 (2012).
- [20] R. C. A. van der Veen, T. Tran, D. Lohse, and C. Sun, Direct measurements of air layer profiles under impacting droplets using high-speed color interferometry, *Phys. Rev. E* **85**, 026315 (2012).
- [21] J. de Ruitter, J. M. Oh, D. van den Ende, and F. Mugele, Dynamics of Collapse of Air Films in Drop Impact, *Phys. Rev. Lett.* **108**, 074505 (2012).
- [22] Y. Liu, P. Tan, and L. Xu, Kelvin–Helmholtz instability in an ultrathin air film causes drop splashing on smooth surfaces, *Proc. Natl. Acad. Sci. USA* **112**, 3280 (2015).
- [23] S. Thoroddsen, K. Takehara, and T. Etoh, Bubble entrapment through topological change, *Phys. Fluids* **22**, 051701 (2010).
- [24] A. Buguin, L. Vovelle, and F. Brochard-Wyart, Shocks in Inertial Dewetting, *Phys. Rev. Lett.* **83**, 1183 (1999).
- [25] M. P. Brenner and D. Gueyffier, On the bursting of viscous films, *Phys. Fluids* **11**, 737 (1999).
- [26] J. E. Sprittles, Air entrainment in dynamic wetting: Knudsen effects and the influence of ambient air pressure, *J. Fluid Mech.* **769**, 444 (2015).
- [27] S. Zhu, A. Yu, D. Hawley, and R. Roy, Frustrated total internal reflection: A demonstration and review, *Am. J. Phys.* **54**, 601 (1986).
- [28] M. Shirota, M. A. van Limbeek, D. Lohse, and C. Sun, Measuring thin films using quantitative frustrated total internal reflection (FTIR), *Eur. Phys. J. E: Soft Matter Biol. Phys.* **40**, 54 (2017).
- [29] See Supplemental Material at <http://link.aps.org/supplemental/10.1103/PhysRevFluids.4.123605> for a detailed description of the revised transfer function with supporting measurements.
- [30] J. D. Paulsen, J. C. Burton, and S. R. Nagel, Viscous to Inertial Crossover in Liquid Drop Coalescence, *Phys. Rev. Lett.* **106**, 114501 (2011).
- [31] S. T. Thoroddsen, T. G. Etoh, K. Takehara, and N. Ootsuka, On the coalescence speed of bubbles, *Phys. Fluids* **17**, 071703 (2005).



- [32] We consider the flow of the air in the thin gap to be viscous due to the thin gap between the droplet and the solid surface. For a typical gap of 100 nm, when the air is driven by the pressure built up in the halo at 0.1 atm over a lateral gap of 100  $\mu\text{m}$ , we estimate a flow velocity of  $\sim 5$  mm/s at the largest, significantly less than the velocities observed in the experiment, implying that the air accumulates in the halo instead of being forced from the gap by the advancing contact line. For air flow at this velocity, the air film volume loses less than 1/100 of its initial value during contact-line propagation over 100 microseconds, consistent with our observation that  $h_{\text{film}}$  is nearly constant during the course of the experiment.
- [33] P.-G. De Gennes, F. Brochard-Wyart, and D. Quéré, Capillarity and Gravity, *Capillarity and Wetting Phenomena* (Springer, New York, 2004).
- [34] A.-L. Biance, C. Clanet, and D. Quéré, First steps in the spreading of a liquid droplet, *Phys. Rev. E* **69**, 016301 (2004).
- [35] A. Vrij, Possible mechanism for the spontaneous rupture of thin, free liquid films, *Discuss. Faraday Soc.* **42**, 23 (1966).
- [36] É. Reyssat and D. Quéré, Bursting of a fluid film in a viscous environment, *Europhys. Lett.* **76**, 236 (2006).
- [37] As viscosity increases, we anticipate that viscous effects will play an increasingly important role; using the contact line velocity and  $\ell_{\text{halo}}$  to calculate the Reynolds number  $Re = vL/\nu = v\ell_{\text{halo}}/\nu$ , we find that the Reynolds number goes from  $\sim 20$  for pure water, down to 0.06 for the 100 cSt solution; the Reynolds number is approximately 1 for the 20 cSt solution.